

X-RAY PRODUCTION IN LASER-HEATED Xe GAS TARGETS

R. L. Kauffman

L. J. Suter

H. N. Kornblum

D. S. Montgomery

Introduction

High-powered lasers focused to high intensities can generate bright x-ray sources. When they directly irradiate high-Z planar targets, more than 50% of the incident laser energy can be converted to soft, or thermal, x rays.^{1,2} Enclosed targets, or hohlraums, can confine the x rays for inertial confinement fusion (ICF) and other radiation-heating experiments.³⁻⁵ Laser-heated plasmas can also be a bright source of keV x-ray emission.^{6,7} These x rays are produced by bound-bound and bound-free transitions in the hot, underdense plasmas. The spectrum is highly structured and depends on the target material.

To date, most studies of x-ray production from laser-produced plasmas have used solid or overdense targets whose initial density, when ionized, is above the critical plasma density, n_c , for absorption.^{1,8} In such targets, the laser energy is absorbed at, or near, critical densities producing a hot plasma. Electron conduction from the hot plasma efficiently heats the higher-density matter while the hot plasma expands to form a lower-density plasma, or corona. This establishes an ablation process in which the denser matter flows through the critical density region and is heated by the laser and then exhausted into the corona. X rays are produced primarily in the region around critical density that is heated by the laser, a region called the conversion layer. For high-Z targets, x rays from the conversion layer can produce a thermal wave into the dense target material, which also can contribute to the production of thermal x rays. Although this heating and x-ray production process has been shown experimentally to be efficient, a significant amount of energy is coupled to hydrodynamic motion of the expanding plasma.

We present results from a new type of target that does not rely on ablation for heating the plasma. In the new targets, the density is less than n_c when ionized. The plasma is initially cold and opaque to the laser.

The laser is absorbed efficiently by inverse bremsstrahlung heating of the plasma. As the plasma is heated, inverse bremsstrahlung becomes less efficient, making the plasma more transparent. The supersonic heat wave that is established ionizes the underdense plasma. The process has the advantage of being more efficient for radiation production, compared with overdense targets, because laser energy heats the plasma without ablation, and less energy is wasted on hydrodynamic motion. The plasma subsequently disassembles as it expands, producing hydrodynamic motion; however, this occurs after the plasma is already heated. The higher plasma temperatures can potentially produce brighter sources for both thermal and multikilovolt x rays. In addition, the higher plasma temperatures can produce higher ionization states, which may result in higher-energy x rays than those attainable using overdense targets. More efficient targets for x-ray production have several applications, including use as a bright x-ray source for backlighters and for radiation-effects experiments.

Experiment

The experiments were performed using the Nova laser⁹ to investigate underdense targets and to demonstrate their efficiency for both thermal and multi-keV x-ray production. The targets, called gasbags¹⁰, are nearly spherical thin membranes filled with gas similar to those developed for large plasma experiments. The thin membranes are made of 4000-Å polyimide ($C_{14}H_6N_2O_4$) stretched over a support washer.¹¹ Figure 1(a) is a picture of the target mounted in the Nova target chamber and viewed from the west by the polar target alignment viewer (TAV1). The striped, nearly hemispherical objects are the membranes. The stripes are caused by interference patterns of the optical illumination system in the membrane. The large black stripe in the center is a support washer for the

(a) Target viewer picture



(b) Schematic

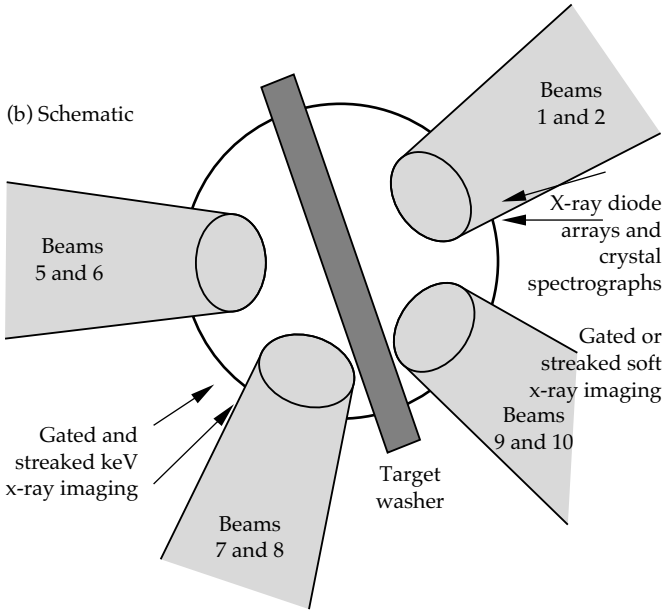


FIGURE 1. Experimental geometry. (a) Image of the target in the target alignment viewer. (b) Schematic of focusing geometry on the target surface and view of the diagnostics. This view is from the west on Nova along the axis of symmetry of the beam cones. (08-00-0296-0438pb01)

membranes. The target is rotated 90° to the normal configuration for the large plasma experiments to allow optimal viewing by x-ray diagnostics.

The targets are filled with a gas mixture of Xe and C₃H₈ (propane) at 1 atm of pressure. We chose Xe because it is a relatively high-atomic-number gas that is easily handled. When ionized to a Ne-like configuration, Xe has x-ray line emission in the 4–6-keV range, which is of interest for x-ray radiography and x-ray exposure experiments. Xe is mixed with C₃H₈ to supply H ions to the plasma. Mixing of light ions, such as H, with heavy ions helps suppress stimulated Brillouin scattering (SBS), which could be a source of energy loss.¹² We chose C₃H₈ because it produces 32 free electrons per molecule when fully ionized. This number is similar to the 44 free electrons per molecule produced

when Xe is ionized to a Ne-like configuration. Thus, the relative concentration of the two gases could be varied without significantly changing the plasma electron density while maintaining the same initial fill pressure.

Table 1 lists the experimental parameters for a total of four Nova shots performed in this first set of scoping experiments. All targets were filled to 1 atm. The varying gas concentrations and approximate diameter of the targets for each shot are listed in the table.

TABLE 1. Summary of Xe-filled gas targets.

Shot number	Gas mixture	E_{Laser} (kJ)	Target diam (mm)	Defocus (mm)	I_{Laser} (W/cm ²)
24061417	25% Xe/ 75% C ₃ H ₈	22.1	2.75	2/5	$1.6/5.5 \times 10^{14}$
24061419	75% Xe/ 25% C ₃ H ₈	20.7	2.75	2/5	$1.5/5.3 \times 10^{14}$
24072917	75% Xe/ 25% C ₃ H ₈	22.1	2.5	1.8	6.7×10^{14}
24072919	90% Xe/ 10% C ₃ H ₈	22.1	2.5	1.8	6.3×10^{14}

The targets are irradiated with eight of Nova's ten beams. Figure 1(b) is a schematic showing the beam positions on the target membrane. The other two Nova beams were not used because they would have hit the target washer support. The beams are pointed at the center of the target. Beams 1, 2, 5, and 6 are at an angle of 43° to the washer normal; beams 7, 8, 9, and 10 are at 63°. The beams irradiate the membrane surface in converging focus. The average intensity on the membrane for each of the shots is listed in Table 1. For the first two shots, the focusing is chosen to provide the lowest intensity irradiation on the membrane and still miss the washer. The average intensity for the beams at 43° is the lower intensity value listed in Table 1; the higher intensity is for the beams incident at 63°. For the second two shots, the focusing is the same for all eight beams so that the average intensity for all beams on the membrane is the same. The laser energy is 21 to 22 kJ of 0.35-μm light in a 1-ns square laser pulse.

We measured x-ray production from the targets using several diagnostics shown in Fig. 1(b). Absolute x-ray production in the range of 0.1 to 1.8 keV is measured using Dante, a broadband, multichannel soft-x-ray spectrometer.¹³ X-ray spectra in the range of 1.8 to 7.0 keV is measured using time-integrated x-ray crystal spectrographs. Absolute yields are obtained by normalizing these spectra to a broadband, filtered x-ray diode on Dante as described below. Beam heating and propagation is measured using gated x-ray imaging.¹⁴ In addition, back-reflected light near the incident wavelength from SBS is measured on beam 7 using the Full Aperture Backscatter Station (FABS).^{15,16}

Results

We studied the heating dynamics of the gasbag using time-resolved, x-ray pinhole camera imaging. Figure 2 is an example of the images taken with the west axial x-ray imager (WAX).¹⁴ This view is the

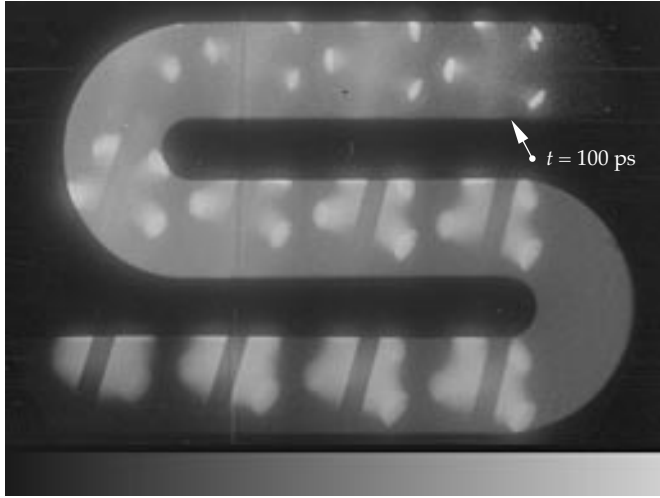


FIGURE 2. Time-resolved x-ray images. The sequence of events is from upper right to lower left. The first image is 100 ps after the beginning of the 1-ns laser pulse. The images are of x-ray emission above 2 keV. Each image is time-resolved to about 80 ps, and time between images in a row is 40 ps. The time interval between the last image in a row and the first image in the next row is 80 ps. (08-00-0296-0439pb01)

same as that shown in Fig. 1(a), although the images are inverted in the pinhole camera. The time sequence of events run from the upper right to the lower left. The time difference between images is ~ 50 ps, and the first image is ~ 100 ps after the start of the laser pulse.

The images show the dynamics of the gasbag heating. Initially, the heating is highly localized at the surface of the gasbag. As the plasma is ionized, the beams penetrate the gasbag until all of the beams reach the center. This event appears to occur in the seventh image, or ~ 400 ps from the beginning of the laser pulse. The beams continue to propagate to the other side of the target. The plasma is still relatively cold since it is not heated by the beams. Later in time, the plasma appears to become more uniformly heated, either by electron or radiation conduction. Late time images viewed from normal to the washer indicate that the entire plasma is heated nearly uniformly by the end of the 1-ns laser pulse.

An interesting feature occurs in the region near the position that the lasers initially irradiate the membrane. This region continues to be brighter even after the laser has penetrated into the center of the gasbag. This appears to be higher-density plasma from a blast wave launched when the initial solid membrane

explodes.¹⁰ The high-density region persists long after the membrane has been ablated, but it should not significantly affect the present experiments.

We measured absolute x-ray production in the 0.1–1.8-keV range using Dante.¹³ Figure 3 shows time-integrated spectra from the three different fill mixtures. The spectra show two distinct features, one at about 270 eV, and the other between 700 eV and 1.5 keV. The highly modulated spectra suggest that the emission is generated mostly by line or band transitions from ionized Xe. High-resolution spectra were not obtained

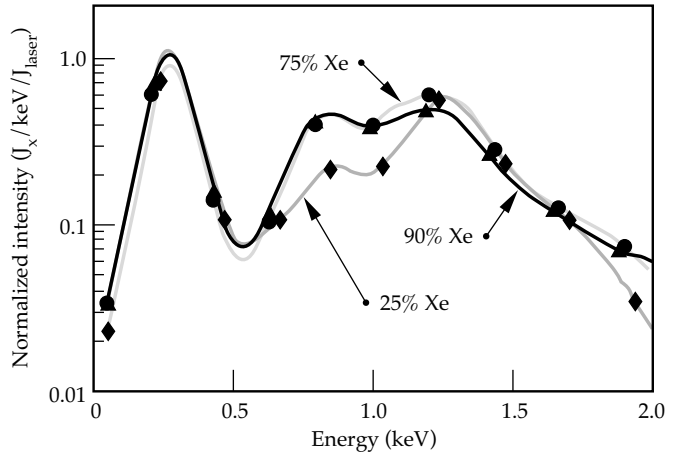


FIGURE 3. Time-integrated x-ray spectrum from 0.1 to 1.8 keV for different concentrations of Xe. (08-00-0296-0440pb01)

below 2 keV, so positive identification of the atomic configurations producing these modulations is not possible. High-resolution spectra of Xe from Tokamak plasmas have identified two spectroscopic regions of line production.¹⁷ In the region from 21 Å (590 eV) to 12 Å (1030 eV), lines and unresolved transition arrays (UTAs) have been identified from Xe^{+26} (Ni-like) to Xe^{+30} (Cr-like) ions. This is approximately the spectral region for the higher-energy feature observed in the present spectrum. The present spectrum is shifted to slightly higher energy probably due to higher plasma temperatures. Reference 17 also reports observing a number of lines from 55 Å (225 eV) to 40 Å (310 eV) and identifies them as $\Delta n = 0$ (3d–3p) transitions from Xe^{+27} (Co-like) and Xe^{+28} (Fe-like). This is the same energy range as the lower-energy feature in the present spectrum. More work is needed to better understand the spectrum below 1.5 keV.

Time-dependent total x-ray power is derived by spectrally integrating time-resolved Dante spectra. Figure 4(a) shows results of the integrals. Time resolution is ~ 180 ps. A typical incident laser pulse summed over all eight beams is also shown. The most distinctive feature in the data is that significant x-ray power

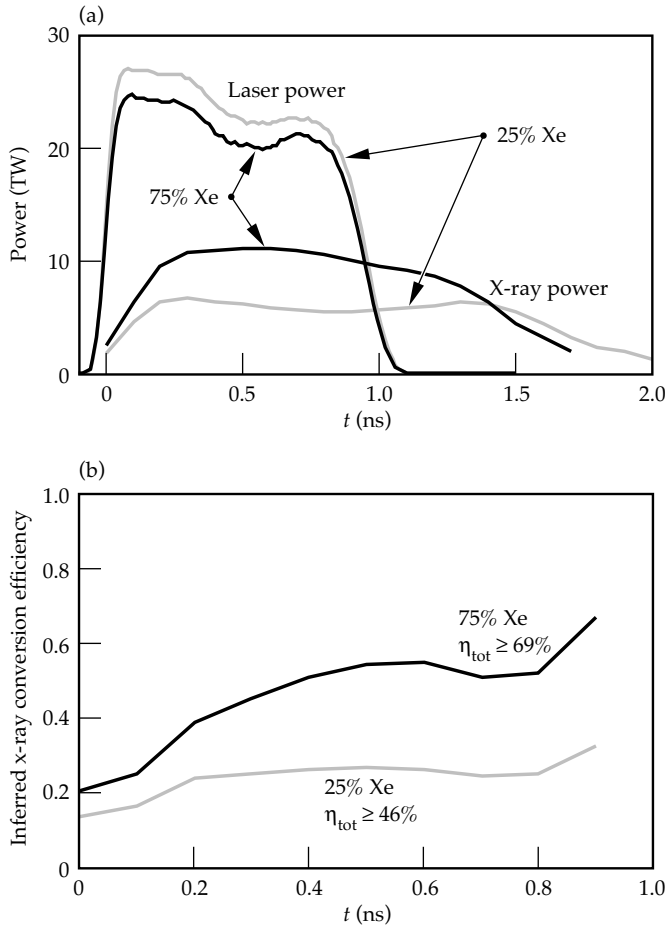


FIGURE 4. X-ray power emitted from 0.1 to 1.8 keV. (a) X-ray and laser power as a function of time. (b) Instantaneous conversion efficiency, defined as the x-ray power divided by the laser power. Data are for 25% and 75% concentrations of Xe. (08-00-0296-0441pb01)

continues 300 to 600 ps after the end of the laser pulse. Errors in timing are estimated to be ~ 100 ps. This observation is consistent with the laser heating the gas as a supersonic heat wave and the cooling occurring later in time due to radiative cooling and hydrodynamic expansion.

Instantaneous x-ray conversion efficiency is derived by dividing the x-ray power by the laser power. Figure 4(b) shows these results. The instantaneous conversion efficiency is $\sim 25\%$ for the 25% Xe fill and varies from 40 to 60% for the 75% Xe fill over most of the laser heating pulse. The instantaneous conversion efficiency begins rising as the laser pulse turns off. Of course, this quantity does not have any significance after the laser pulse ends because the laser power in the denominator is zero. It does, however, indicate that potentially longer pulses can be used, and such pulses can still maintain efficient conversion because there does not seem to be a drop in efficiency during the heating pulse. X-ray production times will ultimately be limited by the disassembly of the target.

Figure 4(b) also shows the total conversion efficiency for x-ray power emitted below 2 keV. These values are higher than the instantaneous conversion efficiency because they include x-ray power emitted after the end of the laser pulse. These efficiencies compare quite favorably with x-ray conversion efficiencies measured from Au disks, as shown in Fig. 5. Here, the Xe data are plotted at the incident intensity on the membrane of the target. The large uncertainty for one of the intensities for the gasbag indicates the range of intensities used with the two different focusings on the membrane. The Au data points are measured conversion efficiencies using single Nova beams irradiating disk targets. The data include the thermal emission from 0.1 to 2 keV and the Au M-band emission from 2 to 5 keV. When contributions are included for the Xe L-shell emission, as discussed below, the Xe gasbags are more efficient emitters than Au disks.

Significant x-ray emission is also observed from $\Delta n = 3-2$ transitions from Xe. Figure 6 shows a typical time-integrated spectrum. The most prominent features are from Xe^{+44} (Ne-like configuration) in the wavelength (energy) range of 2.3 to 3.0 Å (4 to 5 keV). These transitions are identified in Fig. 6. Line emission is also observed between 1.8 and 2.2 Å from $\Delta n = 4-2$ transitions.

Absolute emission levels are obtained by normalizing the spectrum in Fig. 6 to a high-energy channel from Dante. In general, this normalization is within a factor of 2 of the intensity predicted using calibrations of the various spectrograph components. Results of the normalization are plotted in Fig. 7, comparing them with data from various Z disks.¹⁸ The gasbags are significantly more efficient at x-ray production in the 4–5-keV range

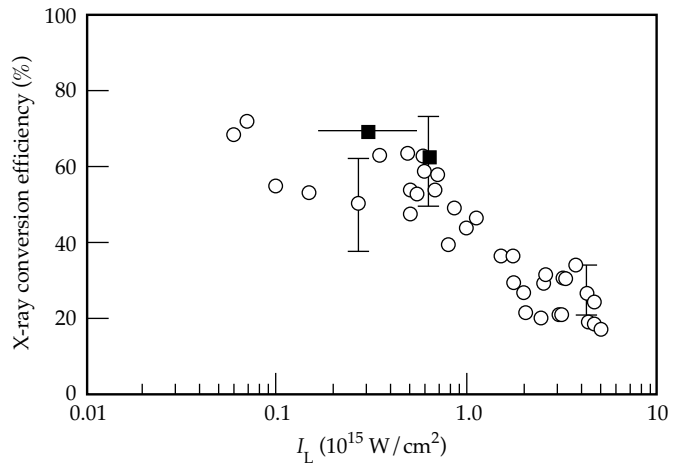


FIGURE 5. Time-integrated x-ray conversion efficiency as a function of intensity for x-ray production in the region of 0.1 to 1.8 keV. Xe data are shown as the closed squares (■). Also shown are data from Au disk experiments (○). Xe experiments are plotted at the average intensity on the initial gasbag surface. (08-00-0296-0442pb01)

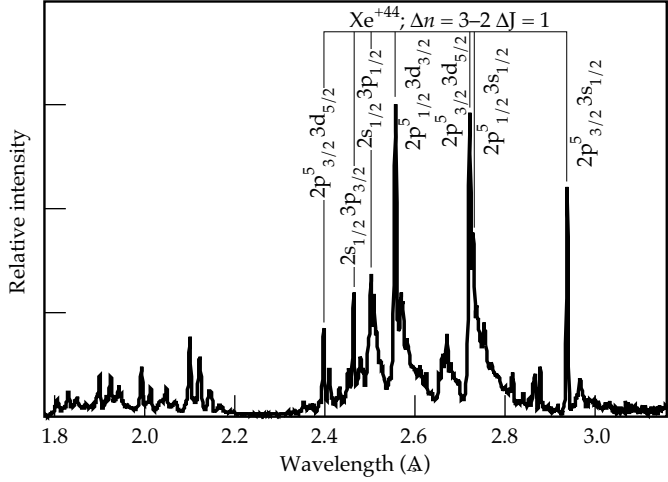


FIGURE 6. X-ray spectrum of Xe for the 4–6-keV region. Resolution is ~ 7 mÅ. Transitions for Ne-like Xe are denoted. (08-00-0296-0443pb01)

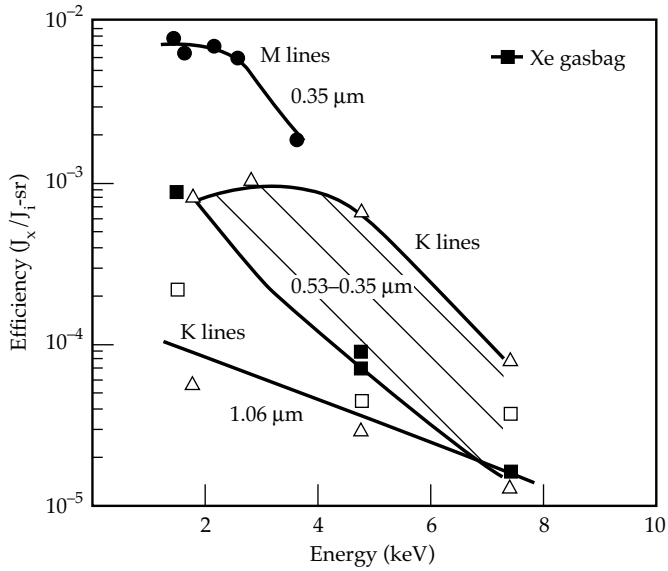


FIGURE 7. X-ray conversion efficiency into multi-keV x rays for Xe gasbags. Data are integrated from 4 to 7 keV. The efficiency is plotted in joules of x rays (J_x) per steradian (sr) divided by the incident laser energy in joules (J_l). The efficiencies are compared with conversion efficiencies measured on solid targets. (08-00-0296-0444pb01)

than disk targets. Only M-shell x-ray production for elements emitting below 3 keV are as efficient.

We monitored backreflected SBS from the gasbags using FABS on beamline 7. As mentioned previously, Xe is mixed with propane to provide hydrogen for enhancing Landau damping of the ion wave produced by SBS.¹² This mechanism has been shown to be effective for suppressing SBS in large-scale plasma experiments.¹⁵ Low levels of SBS are observed for all targets. SBS levels of $\sim 2\%$ are observed for the 25% and 75% Xe fills

at intensities of 4 and 6×10^{14} W/cm², respectively. SBS light scattered outside of the lens was not measured for these experiments, but it has generally been comparable to the light scattered into the lens. These scattering levels are similar to levels seen from hohlraum targets using normal Nova beams.

For the 90%-Xe-filled target, the focus of beamline 7 was placed at the center of the gasbag, and the focal spot on the membrane is ~ 300 μ m in diameter. The intensity of this beam varies from $\sim 3.5 \times 10^{15}$ W/cm² on the membrane to $> 1 \times 10^{16}$ W/cm² at the center of the gasbag. SBS from this shot is $\sim 6\%$, suggesting that SBS will not necessarily be a limiting factor in optimizing the targets for irradiation intensity.

Light produced by stimulated Raman scattering (SRS) was not measured in these experiments. Fast electrons produced by SRS is monitored by measuring the x-ray bremsstrahlung. Inferred fast electron levels are low, typically less than 0.1%. Of course, this does not include fast electrons that escape the target or lose their energy to plasma expansion instead of collisional stopping in the Xe.

Summary

These experiments have demonstrated that underdense targets can be a bright source of both sub-keV and multi-keV x rays. The brightness is greater than that measured in high-Z solid target experiments. Increased x-ray production is attained by reducing the energy coupled to hydrodynamic motion and increasing the internal energy in the plasma. More efficient targets for x-ray production have several applications. One is as a brighter x-ray backlighter source. We have shown that x-ray production is enhanced by a factor of 3 or more above that from conventional solid targets. This factor of 3 directly correlates with lower laser energy requirements for backlighter beams. Spectra at different x-ray energies could be attained by changing the gas or using low-density foams doped with high-Z elements. As long as the ionized electron density of the material is below $\sim 0.25 n_c$, the foam targets should perform similarly to gas-filled targets. At higher density, laser-plasma instabilities become more significant, and at densities above n_c the targets become ablative, performing more like disk targets. Another application is as a bright x-ray source for radiation-effects experiments. In addition, such features could be incorporated into hohlraum designs for ICF to increase radiation production and heating efficiency. Significant work in calculations and experiments is still needed to optimize underdense sources for any of these applications. Nevertheless, these initial experiments demonstrate the significant advantages that underdense target have over solid disk targets as a bright laser-produced x-ray source.

Notes and References

1. W. C. Mead, E. K. Stover, R. L. Kauffman, H. N. Kornblum, and B. F. Lasinski, *Phys. Rev. A* **38**, 5275–5288 (1988).
2. F. Ze, D. R. Kania, S. H. Langer, H. Kornblum, et al., *J. Appl. Phys.* **66**, 1935–1939 (1989).
3. R. Sigel, R. Pakula, S. Sakabe, and G. D. Tsakiris, *Phys. Rev. A* **38**, 5779 (1988).
4. H. Nishimura, Y. Kato, H. Takabe, T. Endo, et al., *Phys. Rev. A* **44**, 8323–8333 (1991).
5. R. L. Kauffman, L. J. Suter, C. B. Darrow, J. D. Kilkenny, et al., *Phys. Rev. Lett.* **73**, 2320–2323 (1994).
6. B. Yaakobi, P. Bourke, Y. Conturie, J. Delettrez, et al., *Opt. Commun.* **38**, 196 (1981).
7. D. L. Matthews, E. M. Campbell, N. M. Ceglio, G. Hermes, et al., *J. Appl. Phys.* **54**, 4260 (1983).
8. R. Sigel, K. Eidmann, F. Lavarenne, and R. F. Schmalz, *Phys. Fluids B* **2**, 199 (1990).
9. E. M. Campbell, J. T. Hunt, E. S. Bliss, D. R. Speck, and R. P. Drake, *Rev. Sci. Instrum.* **57**, 2101 (1986).
10. D. H. Kalantar, B. J. MacGowan, T. P. Bernat, D. E. Klem, et al., *Rev. Sci. Instrum.* **66**, 782 (1995).
11. Luxel Corp., P. O. Box 1879, Friday Harbor, Wash. 98250.
12. E. A. Williams, R. L. Berger, R. P. Drake, A. M. Rubinchik, et al., *Phys. Plasmas* **2**, 129 (1995); H. X. Vu, J. M. Wallace, and B. Bezzerides, *Phys. Plasmas* **1**, 3542 (1994).
13. H. N. Kornblum, R. L. Kauffman, and J. A. Smith, *Rev. Sci. Instrum.* **57**, 2179 (1986).
14. D. K. Bradley, P. M. Bell, J. D. Kilkenny, R. Hanks, et al., *Rev. Sci. Instrum.* **63**, 4813–4817 (1992); P. M. Bell, J. D. Kilkenny, G. Power, R. Bonner, and D. K. Bradley, *Ultra-high Speed and High Speed Photography, Photonics, and Videography '89* (SPIE, Bellingham, WA, 1989; Proc. SPIE, **1155**), pp. 430–444.
15. R. K. Kirkwood, C. A. Back, K. S. Bradley, D. H. Kalantar, et al., *Bull. APS* **39**, 1753 (1994).
16. B. J. MacGowan, et al., *ICF Quarterly Report* **5**(4), 4–220, Lawrence Livermore National Laboratory, Livermore, CA, UCRL-LR-105820-95-4 (1995).
17. F. J. Wyart, C. Bauche-Arnoult, E. Luc-Koenig, and TFTR Group, *Phys. Scr.* **32**, 103–106, (1985).
18. R. Kauffman, *Handbook of Plasma Physics; Vol. 3 Physics of Laser Plasmas*, Eds., A. M. Rubenchik and S. Witkowski (North Holland, Amsterdam 1991), p. 123.